

3D-Printed Stacked Ionic Assemblies for Iontronic Touch Sensors

Jérémy Odent,* Nicolas Baleine, Valentin Biard, Yuta Dobashi, Cédric Vancaeyzeele, Giao T. M. Nguyen, John D. W. Madden, Cédric Plesse, and Jean-Marie Raquez

Sensing is the process of detecting and monitoring any physico-chemical environmental parameters. Herein, new self-powered iontronic sensors, which utilize touch-induced ionic charge separation in ionically conductive hydrogels, are introduced for potential use in object mapping, recognition, and localization. This is accomplished using high-resolution stereolithography (SLA) 3D printing of stacked ionic assemblies consisting of discrete compartments having different ion transport properties. The latter assemblies readily allow programming the output voltage magnitude and polarity by means of variations in ion type, charge density, and cross-linking density within the iontronic device. Voltages of up to 70 mV are generated on application of compressive strains of as much as 50% (≈ 22.5 kPa), with the magnitude directly proportional to stress, and the polarity dependent on the sign of the mobile ion. As a proof-of-concept demonstration, the resulting touch sensors are integrated on the fingertip to enable the tactile feedback, mimicking the tactile perception of objects for recognition applications. In addition, it is proposed that streaming potential is the underlying mechanism behind the iontronic touch sensors. The electromechanical response is therein consistent with a streaming potential model.

1. Introduction

Recent developments in the field of soft robotics and electronics have stimulated efforts toward the fabrication of wearable electromechanical sensors, which transduce external mechanical stimuli into electrical signals.^[1] Robotic-based electromechanical sensors are used in different pressure range, going from low (i.e., <10 kPa, equivalent to gentle touch) to high (i.e., >100 kPa, equivalent to collision with objects) pressure, for detecting biological motion for close proximity human-robot interaction.^[2] Conventional electromechanical soft sensors are mainly resistive^[3] and capacitive^[4] types, transforming the mechanical deformations (i.e., strain or pressure) into real-time electrical variation of resistance and capacitance signals respectively. Different from resistive-type sensors that only exhibit a single layer of active material in the form of percolated elastomer-conductive filler composite, capacitive-type sensors generally require a dielectric layer sandwiched between two soft conducting electrodes.^[1a,5] Piezoelectric-type sensors represent an alternate approach in which a change in electrical polarization inside the material in response to external mechanical load results in a change in surface charge of the material.^[6] Triboelectric-type sensors also represent an interesting alternative where mechanical energy is converted into electricity based on the coupling effect of contact electrification and electrostatic induction.^[7] While these systems are well-studied and vastly available, the main disadvantage of these sensors represents the lack of stretchability in resistive-type sensors, the parasitic noise from the environment in capacitive-type sensors and the charge leakage in piezoelectric-type sensors.^[1b] These sensors have also limited research into the detection of load in multi-dimensional directions so as to emulate any environment.^[1c,8] The requirement of having a power supply for continuous monitoring applications also affects the simplicity and integration of the sensor devices.

Iontronics, in which devices function by coupling electrons with ions to transmit signals as controlled by ionic motion and arrangements, is a recently discovered and fast-expanding technology.^[9] Mobile ions and electrons form an electric double-layer (EDL) at the interface between an ionic conductor and a metal

J. Odent, N. Baleine, V. Biard, J.-M. Raquez
Laboratory of Polymeric and Composite Materials (LPCM)
Center of Innovation and Research in Materials and Polymers (CIRMAP)
University of Mons (UMONS)
Place du Parc 20, Mons 7000, Belgium
E-mail: jeremy.odent@umons.ac.be

C. Vancaeyzeele, G. T. M. Nguyen, C. Plesse
The Laboratory of Physical Chemistry of Polymers and Interfaces (LPPI)
CY Cergy Paris Université
5 mail Gay Lussac, Neuville sur Oise, Cergy 95000, France

J. D. W. Madden
Advanced Materials and Process Engineering Laboratory
Electrical and Computer Engineering
University of British Columbia
Vancouver, BC V6T 1Z4, Canada

Y. Dobashi
Institute of Medical Science
University of Toronto
Toronto, ON M5S 1A8, Canada

 The ORCID identification number(s) for the author(s) of this article can be found under <https://doi.org/10.1002/adfm.202210485>.

DOI: 10.1002/adfm.202210485

electrode, enabling advanced applications including artificial skin^[10] and artificial muscles.^[11] When utilized in wearable capacitive-type sensors by integrating ionic materials (i.e., ionogels and ionic liquids), it enables remarkably elevated capacitance and sensitivity due to the formation of an EDL at the dielectric/ionic conductor interface.^[12] Among these ionic materials, hydrogels are an integral part of living matter that are often invoked in such applications, given that they are stretchable, transparent and ionic conductors that can transmit electrical signals over long distances.^[13] While the majority of examples in the literature refer to electronic conductors, soft ionic conducting layers have been recently and successfully described as efficient electrodes in such devices. Among these examples, Sun et al. created stretchable, transparent, ionic conductors called “ionic skin” using polyacrylamide hydrogel containing sodium chloride salt as the ionic conductor in capacitive-type sensors.^[10a,11a,14] Still, optimizing the performance of hydrogel-based iontronics in electromechanical sensors relies on understanding details of the motion of ions in response to external load.^[1b,13,15] Sawahata et al. found that an electrical potential (in particular a Nernst–Donnan potential) as large as a few millivolts could be generated by a non-uniform mechanical deformation of polyelectrolyte hydrogels, leading to an electromechanical response recently introduced as the piezoionic effect.^[16] In the normal state, backbone (macro)molecules however remain neutral and do not dissociate into positive and negative species. Nonetheless, Erbas et al. further demonstrated that a polyelectrolyte hydrogel's capability to preserve its overall electroneutrality gives rise to significant changes in the electrostatic energies upon deformation (as the translational entropy of counterions decreases).^[17] Prudnikova et al. provided another insight into the piezoionic effect, showing that the compression of polyelectrolyte hydrogels leads to an increase in the osmotic pressure of the gel and thereby to a separation of charges.^[18] Typical piezoionic materials herein consist of a soft polymeric membrane either filled with an electrolyte containing mobile ions (e.g., room temperature ionic liquids or solvated salts) or constituted by a polyelectrolyte containing fixed macro-ions and mobile counterions. The piezoionic effect involves the generation of an output voltage induced by the separation of ions of different mobilities, stimulated by a mechanical load applied to the material.^[15,16b,19] Compared with the currently studied sensors, the unique advantages of piezoionic sensors include self-powered signal generation and the detection of the direction of applied load, which makes them interesting candidates for wearable electromechanical sensing applications.^[20]

As both high sensitivity and high-pressure resolution are demanded for various applications such as robotic manipulation, engineering the sensing, device structure has proven to be an effective method to improve both sensitivity and response speed while simultaneously broadening the pressure responding range in some sensor technologies.^[21] Interestingly, a reverse methodology to typical piezoionic materials (i.e., the potential gradient arises from the lateral pressure applied to the material), in which polyelectrolyte gels with two different degrees of ionization are coupled in a slab geometry (i.e., the ionization is different by design), creates a lateral pressure gradient that results in the buildup of a Nernst–Donnan potential generated at the interface.^[15] This supports the notion that electromechanical responses benefit from structural anisotropy in the material, as the buildup of a Nernst–Donnan potential is the result of non-

uniform generation of dissociating charges. The theory of electrokinetic coupling in charged membranes also suggested other transduction effects such as the occurrence of streaming potential, i.e., the electrochemical potential that develops in response to fluid transport.^[22] Inspired by electric eels, Schroeder et al. created gradients in ion concentration over a number of miniature polyacrylamide hydrogel compartments, bounded by a repeating sequence of cation- and anion-selective hydrogel membranes, that generated ≈ 110 volts at open circuit.^[23] In light of these advancements, additive manufacturing (AM), also known as 3D printing, has become a major player in the fabrication of sensing devices.^[24] While building electromechanical sensors using 3D-printing technology offers new ways to realize the desired spatial arrangement of their components, advancements in multi-process and hybrid 3D printing are leading to the fabrication of sensors that are both geometrically and functionally complex.^[25] Therein, the adaptation of sensing modalities toward the design of unique 3D-printed structures with unusual geometries include innovations on how to miniaturize wearable sensor technologies, how to make them conformal and flexible, as well as tackle the challenges of improving their specificity of detection, sensitivity, simplicity, and integration without any need of external power source.

Here, a strategy of engineering iontronic touch sensors, based on the high-resolution 3D-printing of stacked ionic assemblies consisting of discrete compartments having different ion transport properties, is reported. SLA is the primary technology focus of this work as it provides easy access to individual building layers during fabrication, thus enabling the construction of active 3D structures into complex geometries. Our core technology relies on programming electromechanical gradients by means of variations in ion type, charge density, and cross-linking density within the iontronic devices, so that the ionization is different by design. This breakthrough strategy will not only enable us to address the challenge of building novel self-powered iontronic touch sensors, but also further allow programming directional sensing response with output signal amplification/attenuation by means of multi-compartmental design for discriminative touch sensing and objects localization. As the underlying mechanism behind iontronic touch sensors are still being understood, the mechanism of the observed piezoionic sensor response is discussed. Questions such as “would the interface between anionic and cationic polymers (i.e., variations in ion type) as an ionic p-n junction have an effect on signal amplification?” or “would local modification of the crosslink or charge densities accelerate or slow down ion motion in some direction?” will be addressed. The final result is new iontronic touch sensors, coupled with the knowledge needed to tune their performance to meet the needs of a variety of sensing applications.

2. Results and Discussion

2.1. Fabrication and Properties of 3D-Printed Hydrogel-Based Iontronics

Iontronic sensors for applications in discriminative touch sensing and object localization are herein developed. Rapid fabrication of the proposed sensing device into complex geometries with high-resolution features is performed on an Ember (Autodesk, Inc.) digital mask projection SLA printer, whereby

the photo-pattern is projected through a transparent, oxygen permeable window at the base of a reservoir containing a monomer solution. At first, we 3D-printed a standard non-ionic polyacrylamide (PAAm) hydrogel using acrylamide (AAM) and

N,N'-methylenebisacrylamide (MBA) as cross-linker. The basis for hydrogel-based iontronics arise from direct 3D printing of cross-linked polyelectrolyte hydrogels based on the copolymerization of AAm with ionic co-monomers (**Figure 1A**).

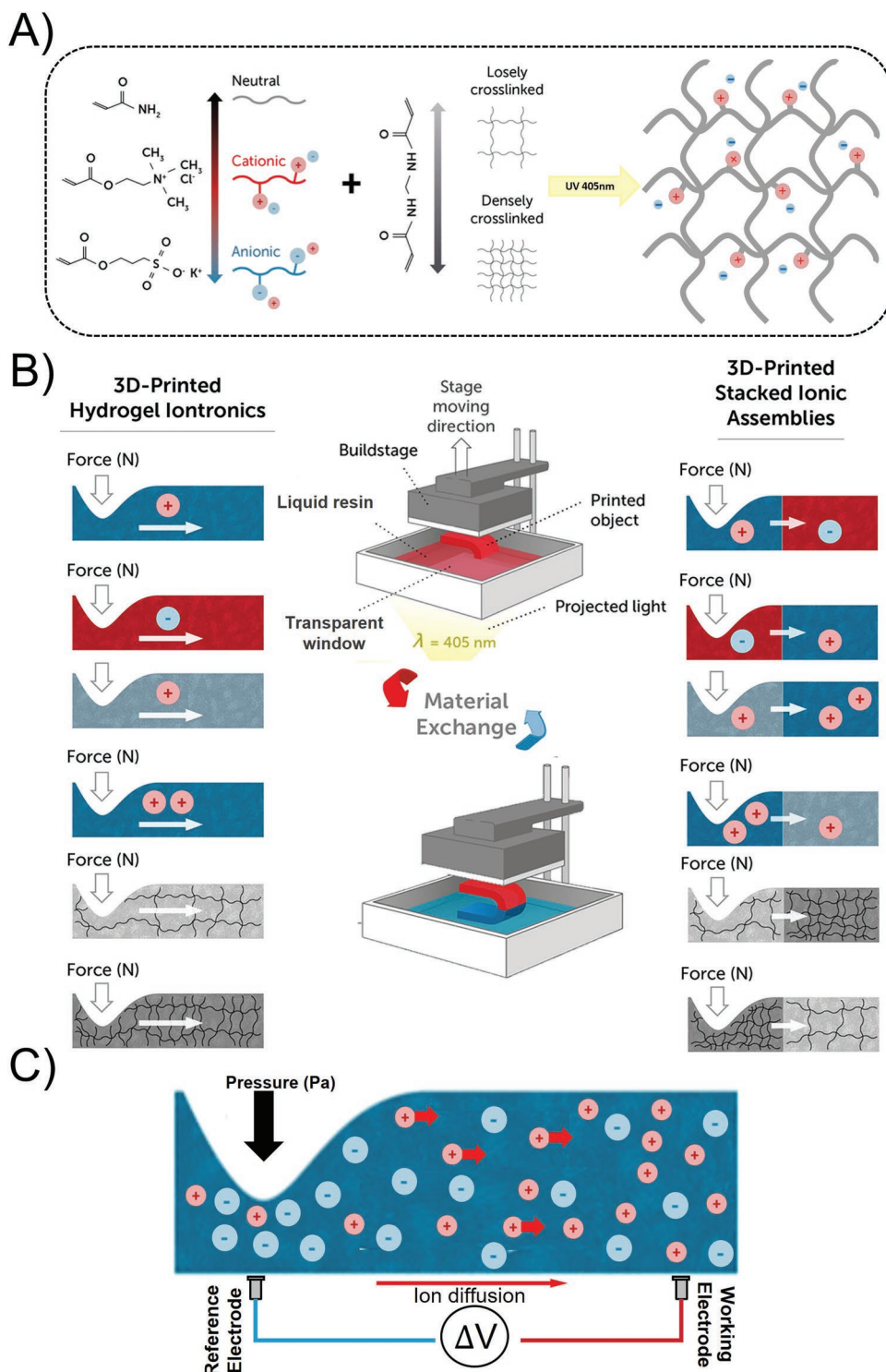


Figure 1. Chemistry and fast bottom-up fabrication of polyelectrolyte hydrogels via copolymerization of AAm with AETA or SPA using MBA crosslinker and TPO photo-initiator A). General strategy toward designing 3D-printed stacked ionic assemblies by means of variations in ion type, charge density, and cross-linking density within the iontronic device via resin vat exchange during the 3D printing process B). C) Schematic of the mechanism behind the as-designed piezoionic touch sensors under indentation, generating charge separation and voltage with respect to the flow of charges from the point of compression (relative to the reference electrode) to the undeformed portion (relative to the working electrode) of the sensor.

3-sulfopropyl acrylate potassium salt (SPA) and [2-(acryloyloxy ethyl)trimethylammonium chloride (AETA) containing mobile potassium (K^+) or chloride (Cl^-) counterions, respectively, are herein selected as ionic building blocks to generate equivalent anionic and cationic PAAm-based hydrogels. Diphenyl(2,4,6-trimethylbenzoyl) phosphine oxide (TPO), a type-I photo-initiator, enables the free radical photo-polymerization of the acrylate groups with near-UV SLA exposure. Overall, photo-rheology provides key data concerning the suitability of these compositions for the 3D printing process by permitting in situ monitoring of chemo-mechanical characteristics during the photo-polymerization reactions (Figure S1 and Table S1, Supporting Information). As the photo-polymerization proceeds, the storage modulus G' increased sharply and then steadily until becoming larger than the loss modulus G'' by an order of magnitude, indicating the photo-induced reactions have reached gelation stages. Compared with neat AAm, the addition of ionic SPA or AETA comonomers leads to markedly faster gelation rates in both the initiation and maturation of gelation. We herein estimated the gel point as the crossover point of G' and G'' , which occurs at ≈ 6 s for non-ionic PAAm and ≈ 4 s for anionic SPA-based and cationic AETA-based counterparts (see Table S1, Supporting Information). A three order of magnitude increase in complex viscosity within short near-UV exposure time (≈ 10 s) for the various materials further represents a key feature for the rapid fabrication of macroscale objects using commercial SLA technology. As water evaporation from hydrogel-based iontronics is a particularly important obstacle in sensing applications and that encapsulation is not an option,^[26] water is partly substituted by the less volatile glycerol, simply by soaking the hydrogel in a glycerol/water (75/25 wt.%) solution to reach a swelling ratio of 50%. Mass loss experiments revealed that the replacement of water with the non-volatile glycerol/water solution resulted in ionically conductive gels that are stable in air (Figure S2 in the Supporting Information). Oscillation amplitude sweeps of the resulting materials provided additional information concerning their rheo-mechanical characteristics, attesting a typical elastic solid behavior since G' in each case is higher than G'' (Figure S3 and Table S2 in the Supporting Information). The linear viscoelastic region can be identified in the region where G' is independent of the applied deformation, showing no changes to the integrity and microstructure of the materials when subjected to small amplitude oscillation conditions (up to $\approx 20\%$ strain, hereunder referred as Regime I). An estimation of the effective cross-linking density (ν_e) is further attempted by modulus measurements in the rubbery plateau region given the $\nu_e = G'/RT$ equation.^[27] Similar crosslink densities are observed on the various materials containing the same amount of MBA crosslinker ($\approx 10^{-6}$ mol cm^{-3} at 1 mol% MBA, see Table S2, Supporting Information). Additionally, the resulting 3D-printed structures are not only optically transparent, with a transmission coefficient of $\approx 85\%$ from 400–800 nm (Figure S4, Supporting Information) but also ionically conductive since SPA and AETA comonomers are integrated with their mobile counterions, K^+ and Cl^- respectively (Table S3, Supporting Information). While the incorporation of potassium chloride salt (KCl, 2 M) into standard non-ionic PAAm hydrogel endows the material with an ionic conductivity of $\approx 1.9 \times 10^{-4}$ S cm^{-1} , higher ionic conductivity is recorded for anionic SPA-based and cationic

AETA-based counterparts with no extra KCl salt added ($\approx 6.5 \times 10^{-4}$ and 7.1×10^{-4} S cm^{-1} at 30 mol.% of SPA and AETA, respectively). The ionic conductivity also increases with the content of ionic comonomers but decreases with the MBA crosslinker content (see Table S3, Supporting Information).

2.2. Electromechanical Responses and Underlying Mechanisms

When utilized in touch sensing applications, hydrogel-based iontronics generated an output voltage in response to mechanical deformation. Under indentation, an initial viscoelastic deformation entrains the mobile counterions to flow from the point of compression, generating a charge imbalance within the hydrogel together with mirror charges in the metal electrodes (Figure S5, Supporting Information). In the indentation experiments, a reference (ground) electrode is placed under the indented portion, whereas a working (sense) electrode is placed in the undeformed portion of the hydrogel. This leads to the interpretation of the voltage resulting from compression is cationically driven (i.e., preferential displacement of the cations) if it is positive, and anionically driven (i.e., preferential displacement of the anions) if it is negative (Figure 1C). The sensors exhibited instantaneous response to perturbations and returned toward their initial value in a strain follower configuration (Figure S6, Supporting Information). The materials show good signal stability over 10 cycles (Figure S7, Supporting Information). As a first demonstration, we compared the electromechanical responses of as-designed anionic SPA-based and cationic AETA-based PAAm hydrogels with standard PAAm hydrogels containing additional KCl salt (Figure S8, Supporting Information). The polarity of output voltages is herein consistent with movement of the mobile counterions away from the indented region. As a consequence, positive and negative voltages respectively arise from anionic SPA-based and cationic AETA-based PAAm hydrogels, whose charge is balanced by K^+ cations and Cl^- anions respectively. In contrast, the positive output voltage within standard PAAm/KCl hydrogels suggests that K^+ cations are more mobile (i.e., faster expulsion upon mechanical deformation) in the present situation than Cl^- anions, in accordance with some previous observations.^[28] The imbalance of the ion distribution is consistent with the hydration shell radius of ≈ 0.138 and ≈ 0.181 nm respectively for K^+ and Cl^- ions,^[29] suggesting that there may be some drag from the hydrogel matrix acting on the ions. When the mechanical deformation is held constant, though, the imbalanced cation and anion distributions are transient, causing voltage decay within standard PAAm/KCl hydrogels (Figure S9 in the Supporting Information, showing responses to 18% compression held for 100 s). By contrast, much less decay is observed for anionic SPA-based and cationic AETA-based counterparts (see Figure S9 in the Supporting Information). The latter results are consistent with the presence of fixed macro-ions and their associated mobile counterions, which allow the ion separation to persist at longer times, and permanently as predicted upon the Donnan effect.^[19b]

The generated output voltage amplitude is also found to increase as greater mechanical deformation is applied, consistent with the so-called piezoionic effect, where a mechanical

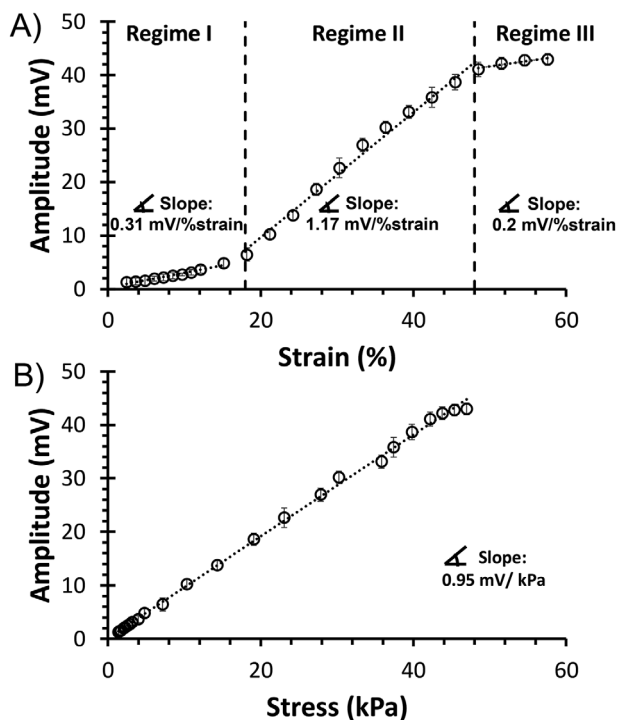


Figure 2. Output voltage amplitude as a function of the compressive strain A) or stress B) applied for PAAm-based hydrogels containing 1 mol.% MBA and 30 mol.% SPA.

perturbation induces ionic charge separation.^[15–19] The deformation mechanics fall into three regimes that are consistent with the viscoelastic behavior of the materials under applied compressive strain (Figure 2A). Regime I (up to ≈20% strain) shows a simple proportionality between voltage and strain, corresponding to the linear region of the stress-strain curve. Regime II (within ≈20–50% strain) has a much steeper slope in response, while Regime III (over ≈50% strain) suggests a near saturation. The electromechanical response is consistent with a streaming potential model over the entire range of strains, showing direct proportionality between voltage and pressure difference (Figure 2B), as is now discussed.

In the linear viscoelasticity regime of small to moderate deformations, the output voltage amplitude shows a linear rise with the imposed strains (see Regime I in Figure 2A). The pressure gradient that develops across the sensor produces unequal distribution of charged ions that results in the buildup of a potential difference. Using the analytical models, we found that the experimental response is reasonably approximated by the Nernst–Donnan response at small deformations, whereas the streaming model provides a better representation across the entire range (Figure S10, Supporting Information). The Nernst–Donnan response is given by:

$$\Delta V_{\text{Donnan}} = \frac{kT}{e} \ln \frac{C_{\text{indent}}}{C_{\text{bulk}}} \quad (1)$$

where C_{indent} is the concentration of immobile ions under the indenter, C_{bulk} is the concentration of immobile ions away from the indenter, k is Boltzmann's constant, T is absolute

temperature, and e is fundamental charge (with $kT/e \approx 25$ mV at ambient temperature). The polymer density is higher in the indented region, so that when the flow is complete, the concentration of electrolyte is increased by $1/(1-\epsilon)$, where ϵ is compressive strain. The local slope of the electromechanical response is then:

$$\frac{\Delta V_{\text{Donnan}}}{\Delta \epsilon} = \frac{kT}{e(1-\epsilon)} \quad (2)$$

Using anionic SPA-based PAAm hydrogels (i.e., 30 mol.% SPA, 1 mol.% MBA) whose charge is balanced by mobile K^+ counterions, we found that the slope of the sensor voltage response in Regime I is of 0.31 mV/%strain. The latter experimental result nearly matches the 0.33 mV/%strain expected from Equation (2), within the limit of small strain, but otherwise underestimates the response. Herein, the sign of the response is consistent with movement of the K^+ cations away from the indented region. At larger deformation, beyond Regime I (see Regime II in Figure 2A), the Nernst–Donnan model fit is tending to be increasingly inappropriate, and does not provide an adequate description. Within the relatively short timescales of the tests performed in this work, the Donnan model greatly underestimates the response, and is not appropriate for measuring peak voltage generation. However, streaming potential combined with the mechanics of indentation provides an alternative explanation for the observed responses. In streaming, we expect that the current generated is proportional to pressure gradient. Using the Finite Element Method, we found that the pressure gradient is not linearly proportional to indenter displacement (Figure S11, Supporting Information). It rises relatively slowly in Regime I (Video S1, Supporting Information), then faster in Regime II (Video S2, Supporting Information), and finally more slowly in Regime III (Video S3, Supporting Information), whereby hydrogel flow is likely induced. Taking into account the non-linear mechanics of indentation, plotting voltage generated versus stress instead of strain straightens out the curve, showing a linear response (see Figure 2B). The direct proportionality suggests a streaming potential model, in which transient charge separation rate increases linearly with the pressure difference. The driven convection of charged electrolyte is balanced in a steady state by the migration and diffusion-driven reverse current. Assuming Darcy flow and domination of convection current, the streaming potential is then given by:

$$V_{\text{Streaming}} = \frac{L}{\sigma} \Delta P = \frac{Ne}{\eta} \frac{\kappa}{\sigma} \Delta P \sim \frac{6\pi r \kappa}{e} \Delta P \quad (3)$$

where ΔP is the pressure difference at open circuit, L is the coupling coefficient between pressure and current, κ/η is the ratio of permeability to viscosity, N is the concentration of ions in numbers per cubic meter, σ is the ionic conductivity and e is the fundamental charge.^[22b] Assuming Stoke's drag for ions of effective radius, r , the streaming equation becomes a function of the ion size and the permeability.^[22a,30] Based on the fit slope of 0.95 mV kPa⁻¹ in Figure 2B, and a solvated ion size of 0.14 nm, the estimated permeability is 10⁻¹⁵ m², being large, but remains within the range commonly reported for polyacrylamide.^[31]

The local slope of the electromechanical response thereby rises much faster in Regime II than expected from Equation (2). In the poroviscoelastic hydrogels, we expect that increase in the effective deformed area yields a prolonged poroelastic relaxation time, contributing to a steeper slope of response (see Regime II in Figure 2A). However, the proportionality between load and voltage is evident (see Figure 2B). In the high-strain Regime III, the electromechanical response saturates (see Regime III in Figure 2A). Under very high mechanical loading conditions, the polymer matrix itself is likely flowing. Interestingly, the proportionality between voltage and pressure difference still holds quite well, again suggesting that a streaming-like model is appropriate to describe the electrochemical response. Zhu et al. have therein shown that the magnitude and response speed of voltage in ionic materials is decided not only by ions properties but also by water migration.^[32] Generally, the forward movement of mobile ions and water molecules toward the outside electrode (i.e., having lower hydraulic pressure) generates a concentration gradient and built-in electrical field in the ionic materials. Voltage decay is seen at longer times, as the water swells the polymer in the low-pressure region, creating an elastic counter pressure that slows convection. The voltage difference drives the migration of ions back toward the inside electrode, causing a voltage decay. Overall, the electromechanical response appears to be largely explained by the non-linear poroviscoelastic behavior of resulting hydrogels.

We extend our investigation to the generated output voltage amplitude by varying charge density (from 0 to 50 mol%) and cross-linking density (0.1–5 mol.%) of the anionic SPA-based PAAm hydrogels (Figure 3). Once again, the direct proportionality between voltage and pressure difference is found. What is new is that the higher the hydrogel fixed charge density, the higher the amplitude of the output voltage (Figure 3A). For instance, the output voltage of the anionic hydrogels increases from ≈ 4 to 68 mV (i.e., 17-fold increase) between 10 and 50 mol.% SPA at 1 mol.% MBA when subjected to a 20 kPa stress stimulation. Higher charge density means more corresponding mobile counterions, and hence larger streaming currents. The cross-linking density, with respect to the amount of MBA cross-linker, is another differentiator. As a consequence, the higher the hydrogel cross-linking density, the lower the amplitude of the output voltage (Figure 3B). For instance, the output voltage of the anionic hydrogels decreases from ≈ 20 to 1.5 mV (i.e., 13-fold decrease) between 1 and 5 mol.% MBA at 30 mol.% SPA when subjected to a 20 kPa stress stimulation. This inverse dependence makes sense from a streaming perspective, as the increased cross-linking also increases the resistance to electrolyte motion within the materials.

Resulting hydrogel-based iontronics not only detect touch but also further integrate real-time object recognition and localization. Object recognition is equivalent to determining the object-specific map while the localization refers to finding the precise position of a contact point in the local sensor frame. The recognition approach is herein validated upon the discrimination of cylindrical objects of outer diameters 4 and 6 mm (Figure S12 in the Supporting Information). As a result, the output voltage profile changes with varying the indenter geometry, providing an assessment of the many dimensions of an indentation formed under controlled conditions. In addition,

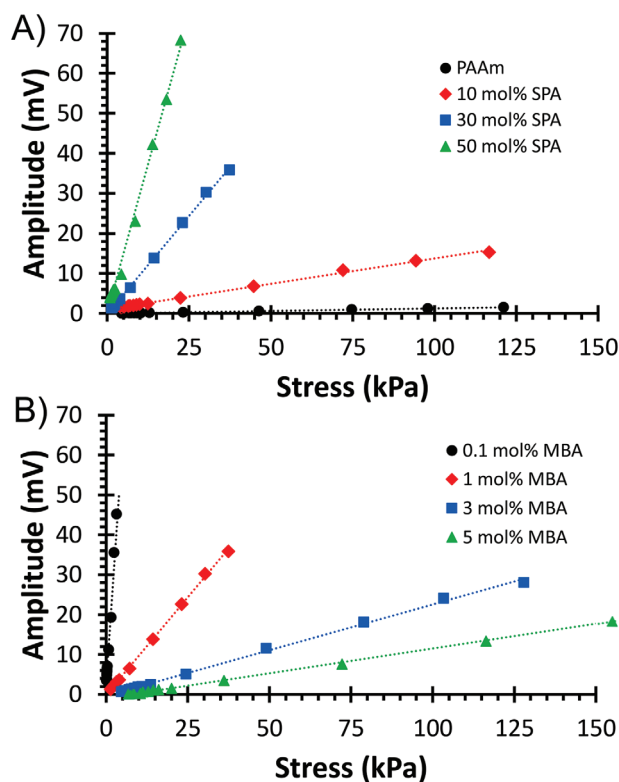


Figure 3. Output voltage amplitude as a function of the stress applied for standard PAAm hydrogels (black circles) and corresponding PAAm-based hydrogels containing 1 mol.% of MBA and 10 mol.% (red diamonds), 30 mol.% (blue squares) and 50 mol.% (green triangles) of SPA A) as well as 30 mol.% of SPA and 0.1 mol.% (black circles), 1 mol.% (red diamonds), 3 mol.% (blue squares), and 5 mol.% (green triangles) of MBA B).

the location of the touch determines the sign of the output signal (Figure S13 in the Supporting Information). Pressing on the right hand side leads to a positive response voltage, while the left hand side produces an equal but opposite response. This makes sense since the pressure gradient and ion flow are reversed, and provides additional information from each electrode pair.

2.3. 3D-Printed Stacked Ionic Assemblies and Practical Demonstration

The possibilities and limitations of the versatile SLA platform to generate desired structural assemblies on the generation of form are further explored during the high-resolution 3D printing of our proposed sensing device. Three separate strategies for developing very smooth gradients by means of variations in ion type, charge density, and cross-linking density within the SLA-printed iontronic device are accordingly demonstrated, so that the piezoionic behavior is different by design. The approach involves the simple exchange of the photo-curable formulation within separate resin reservoirs to get different purposely selected materials during fabrication in order to generate structural anisotropy within the final 3D-printed object (Figure 1B). Resin-replacement herein enables compositional

changes between each individual building layers, leading to a patterned structure whereby the chemical composition of the structure changes stepwise along the printing Z-axis. Using this approach, 3D-printed ionic assemblies consisting of a two-compartment system made of discrete layers containing different ion type (i.e., SPA versus AETA at 30 mol.% and 1 mol.% MBA), charge density (i.e., 10 mol.% versus 50 mol.% SPA and 1 mol.% MBA) and cross-linking density (i.e., 1 mol.% versus 5 mol.% MBA and 30 mol.% SPA) are fabricated (see Figure 1B). Recall that the polarity of output voltages is consistent with movement of the mobile counterions away from the indented region, knowing that the generated output voltage amplitude is found to be proportional to the hydrogel charge density and inversely proportional to the hydrogel cross-linking density. Our resulting 3D-printed stacked ionic assemblies therein preserve the dependence of the voltage polarity on the location of the perturbations. In other terms, positive and negative voltages respectively arise when the indented compartment corresponds to the anionic or the cationic counterparts whose charge is balanced by K^+ cations and Cl^- anions respectively. By contrast, resulting two-compartment assemblies readily allow programming the signal magnitude of the iontronic sensors with respect to the flow of excess charges from the indented compartment to the neighboring compartment of different ion transport properties (Figure 4).

3D-printed stacked ionic assemblies made of discrete anionic and cationic compartments containing equal numbers of ions (i.e., SPA vs AETA at 30 mol.% and 1 mol.% MBA) lead to an output signal attenuation wherever the indented compartment is the anionic or the cationic counterparts (Figure 4A). For instance, a 3.3-fold decrease (i.e., ≈ 23 –7 mV) in the output voltage amplitude is recorded when the anionic compartment is subjected to a 20 kPa stress stimulation (i.e., leading to a flow of excess charges from the anionic to the cationic counterparts). However, applying a 20 kPa stress stimulation to the cationic compartment (i.e., leading to a flow of excess charges from the cationic to the anionic compartment) lead to a 2.3-fold decrease (i.e., from ≈ -12 to -5 mV) in the output voltage amplitude. The latter results are consistent with movement of mobile ions away from the indented region and their neutralization with complementary counterions at the junction between the anionic and the cationic compartments. The difference in the recorded output signal amplitude when the anionic or the cationic compartment is stimulated (i.e., 3.3-fold vs 2.3-fold decrease with respect to the flow of K^+ cations or Cl^- anions respectively) is herein consistent with the faster expulsion of K^+ cations than Cl^- anions upon mechanical deformation. By contrast, 3D-printed stacked ionic assemblies of different charge density and cross-linking density not only influence the output voltage amplitude but also the direction of the voltage according to the position of each compartment during mechanical stimulation (see Figure 4). Specifically, the anionic SPA-based assemblies consisting of two compartments having different charge density (i.e., 10 mol.% vs 50 mol.% SPA and 1 mol.% MBA) lead to an output signal amplification when the indented compartment has the lower charge density (Figure 4B). For instance, a four-fold increase (i.e., ≈ 4 –16 mV) in the output voltage amplitude is recorded when the compartment of lower charge density is subjected to a 20 kPa stress stimulation (i.e., leading to a flow

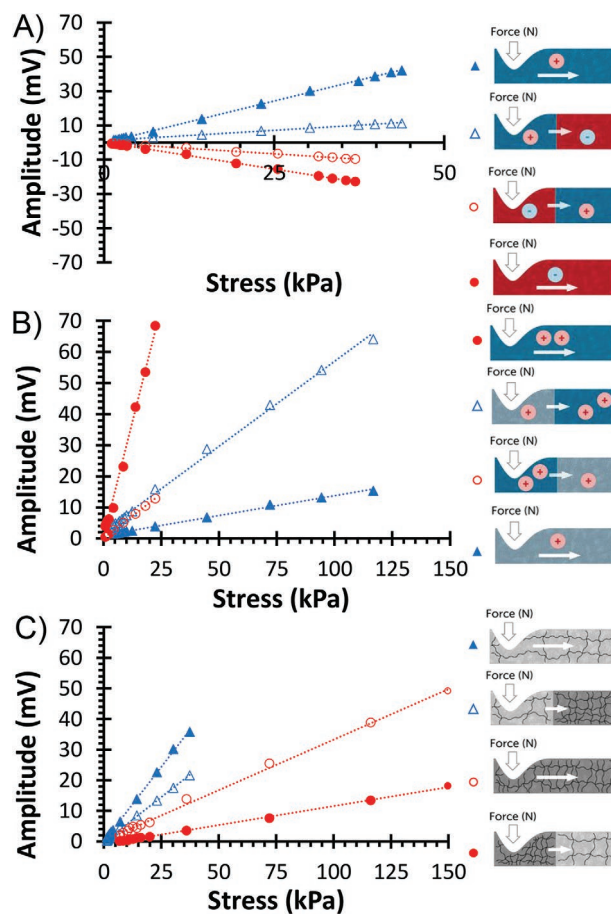


Figure 4. Output voltage amplitude as a function of the stress applied for 3D-printed stacked ionic assemblies consisting of two-compartment having different ion type (A, i.e., SPA versus AETA at 30 mol.% and 1 mol.% MBA), charge density (B, i.e., 10 mol.% versus 50 mol.% SPA and 1 mol.% MBA) and cross-linking density (C, i.e., 1 mol.% versus 5 mol.% MBA and 30 mol.% SPA). Electromechanical performances are compared with their respective single-component materials.

of excess charges from the 10 mol.% to the 50 mol.% SPA). By contrast, an output signal attenuation is found when the indented compartment has the higher charge density. Herein, a 5.3-fold decrease (i.e., ≈ 68 –13 mV) in the output voltage amplitude is recorded when the compartment of higher charge density is subjected to a 20 kPa stress stimulation (i.e., leading to a flow of excess charges from the 50 mol.% to the 10 mol.% SPA). Overall, the output voltage amplification (or attenuation) is consistent with movement of mobile ions away from the indented compartment of lower charge density (or higher charge density) to the neighboring compartment of higher charge density (or lower charge density). Similarly, the anionic SPA-based assemblies consisting of two compartments having different cross-linking density (i.e., 1 mol.% vs 5 mol.% MBA and 30 mol.% SPA) lead to an output signal amplification or attenuation when the indented compartment has the lower or the higher cross-linking density respectively (Figure 4C). For instance, a 1.8-fold decrease (i.e., from ≈ 23 to 13 mV) in the output voltage amplitude is recorded when the compartment of lower cross-linking density is subjected to a 20 kPa stress

stimulation (i.e., leading to a flow of excess charges from the 1 mol.% to the 5 mol.% MBA). However, applying a 20 kPa stress stimulation to the compartment of higher cross-linking density (i.e., leading to a flow of excess charges from the 5 mol.% to the 1 mol.% MBA) lead to a 4.2-fold increase (i.e., $\approx 6\text{--}1.5$ mV) in the output voltage amplitude. Again, the output voltage amplitude amplification is consistent with movement of mobile ions away from the indented compartment to the neighboring compartment of higher cross-linking density, while the output voltage amplitude attenuation is consistent with movement of mobile ions toward the compartment of lower cross-linking density.

The responses seen in the stacked assemblies can be explained by the flow of solvent and ions that occurs when the sensor is indented. Under applied compressive strain, there is a pressure gradient normal to the indentation direction that extends out to ca. twice the indenter diameter (see Figure S11, Supporting Information). This drives flow and carries charge perpendicular to the indentation, as well as into the neighboring region. In the case of the anionic/cationic structure, the gradient within the oppositely charged region will create an opposing current, reducing the generated voltage. It will also create an additional voltage difference at the interface between the anionic and cationic regions, further reducing sense voltage, and explaining why a smaller magnitude of response is seen when regions of opposing charge are placed side by side (see Figure 4A). In the case of combined low and high concentrations, once again flow will extend across the boundary between the regions. The high concentration region is known to produce a larger voltage, presumably because solvent flow carries more ions with it (see Figure 4B). This charge transfer will be reduced where there is a lower concentration of balancing ions. Additional cross-linking is known to reduce voltage, again likely due to a drop in streaming current. As a result, the addition of regions of high cross-link density are expected to reduce sensitivity, as is observed (see Figure 4C). Overall, sensitivity is reduced when charge flow is decreased by increasing resistance to flow after cross-linking, by reducing the current using lower ion concentrations, and by having a reversal in polarity, setting up oppositely charged regions side by side.

Inspired by the functions of the human fingertip, we thereby fabricated artificial fingerprint-like patterns with tactile feedback, mimicking the tactual feeling perceived from the finger, i.e., when touching the highly touch-sensitive skin or the much less sensitive fingernail. As proof-of-concept demonstration, curved finger sleeves consisting of two-compartment assemblies having different charge density are 3D-printed, connected end-to-end with electric connections, and adapted to a wearer (Figure 5; Figure S14, Supporting Information). In the present situation, the sensitive skin (i.e., bottom part of the sleeve) and the insensitive fingernail (i.e., upper part of the sleeve) are respectively made of compartments of low and high charge density (i.e., 10 mol.% vs 50 mol.% SPA and 1 mol.% MBA). Immediately after contact, the artificial fingertip exhibited highly touch-sensitive in response to perturbations when the bottom part of the sleeve is indented. By contrast, the upper part of the sleeve, corresponding to the fingernail, is not responding (or very slightly)

to touch. The latter response is further confirmed over multiple touch stimulation (see Figure 5).

3. Conclusions

This paper reports the high-resolution, stereolithography 3D-printing of brand-new, self-powered iontronic touch sensors for use in object recognition, localization, and activity monitoring. The core technology of this work relies on designing 3D-printed stacked ionic assemblies consisting of two-compartment systems with different ion type, charge density, and cross-linking density, so that the piezoionic behavior is different by design. The composition of these electromechanical gradients can be controlled during the 3D printing process by simply exchanging the photo-curable formulation within separate resin reservoirs. The resulting iontronic sensors exhibited instantaneous response to perturbations and returned toward their initial value in a strain follower configuration. Although the deformation mechanics fall into three regimes that are consistent with the viscoelastic behavior of the materials under applied compressive strain, the nearly perfect proportionality between voltage and pressure difference provides a compelling description of the response over the entire range of strains. The entire response is consistent with a streaming potential model. The polarity of output voltages is consistent with movement of the mobile counterions away from the indented region. The generated output voltage amplitude at a given applied pressure is found to be approximately proportional to the hydrogel charge density and inversely proportional to the hydrogel cross-linking density. As a result, the resulting two-compartment assemblies readily allow programming the signal magnitude (i.e., leading to a controlled output signal amplification or attenuation) of the iontronic sensors with respect to the flow of excess charges from the indented compartment to the neighboring compartment of different ion transport properties. The resulting tactile sensors also exhibit sensitive touch-pressure monitoring and localization for activity recognition applications, simplifying the relevant sensing systems and favoring integration for applications such as 3D-printed artificial fingertips. In particular, our work is a platform for designing other highly sensitive and wide-detection range pressure (from \approx few kPa to 150 kPa) sensors constructed on 3D-printed hierarchical functional structures for use in a wide range of technological applications.

4. Experimental Section

Materials: AAm (99%, Sigma–Aldrich), AETA (80 wt.% in H₂O, Sigma–Aldrich), SPA (99%, Sigma–Aldrich), MBA (99%, Sigma–Aldrich), TPO (97%, Sigma–Aldrich), KCl (Acros) were purchased as indicated and used without further purification.

Preparation and 3D Printing of Hydrogel-Based Iontronics: AAm, AETA, and SPA monomers together with MBA cross-linker at different ratios were dissolved in a solution of methanol and deionized water (75/25 wt.%) to reach a final monomer-to-solvent ratio of 1:3. The final addition of 0.5 mol.% of TPO, a type-I photo-initiator, enables free radical photo-polymerization of the acrylate groups with near-UV SLA exposure. For this work, an Ember by Autodesk desktop 3D printer was used. This 3D printer was provided with a LED projector ($\lambda = 405$ nm) with an

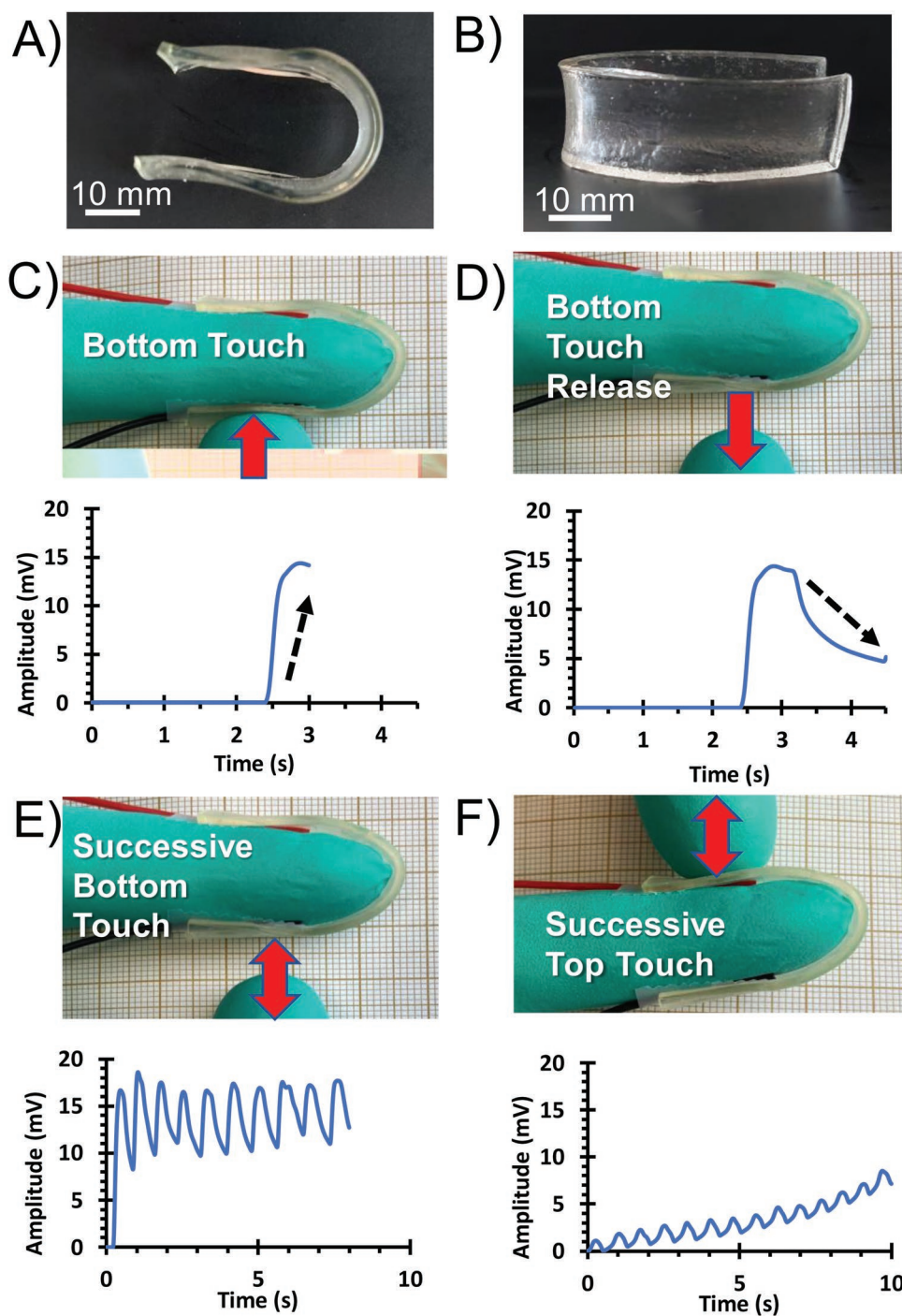


Figure 5. 3D-printed artificial fingerprint-like sleeve (A, i.e., top view and B, i.e., side view, dimensions: $30 \times 10 \times 1.5 \text{ mm}^3$) with tactile feedback mimicking the tactual feeling perceived while either touching (C, i.e., simple touch and E, i.e., successive touch) and releasing (D) the highly touch-sensitive skin (i.e., bottom part of the sleeve) or the much less sensitive fingernail (F, i.e., successive touch on the upper part of the sleeve).

irradiance of $E_e = 22.5 \text{ mW cm}^{-2}$ and is controlled by an open-source modeling software. All the .stl files were designed on the Autodesk Fusion 360 modeling software and then imported on Autodesk Print Studio which modified and sliced the design into discrete $100 \mu\text{m}$ layers. The resulting sliced image and the corresponding actions for the 3D printer were then loaded on to the Ember 3D printer. Short layer times exposure ($t = 4\text{ s}$ per $100 \mu\text{m}$ layer) were used in this study leading to high resolution objects. Stacked ionic assemblies were obtained by simple exchange of

the photo-curable formulation within separate resin reservoirs during fabrication. The resulting 3D-printed materials were then soaked into glycerol/water solution (75/25 wt.%) to reach a constant swelling ratio of 50% prior any further uses.

Photo-Rheology. The in situ monitoring of the photo-polymerization as a function of light illumination was carried out using a rheometer MCR 302 (Anton-Paar) combined with a UV-light source OmniCure S1000 (Lumen Dynamics) and UV filter ($\lambda = 400\text{--}500 \text{ nm}$). This study used a transparent

circular parallel plate (diameter = 25 mm) with a gap of 1 mm through constant frequency (1 Hz) and amplitude (1%) oscillatory shear during photo-exposure. The irradiance of the light source was fixed at 22.5 mW.cm⁻².

Sensing Characterization: The piezoelectric touch sensors were placed within a 3D-printed rectangular support structure embedding two electrode strips of 1 mm diameter separated by 10 mm. The reference (ground) electrode was systematically placed under the indented portion, whereas the working (sense) electrode was placed in the undeformed portion of the sensor. The electrodes were connected to an electromechanical workstation (Interface 1010e potentiostat, Gamry Instruments) set in open circuit voltage to measure the potential difference at the two electrodes. While the resulting 3D-printed support material was placed in a tensile machine Ametek LS1 (Lloyd Materials) on the lower clamp, a 3D-printed cylindrical indenter of outer diameter 4 mm was set on the upper clamp right on top of the reference electrode. Under indentation, a preferential displacement of the cations over anions results in a positive voltage reading, and vice versa. Overall, the signal stability was evidenced through cyclic compression tests by repeatedly load and unload to $\epsilon = 18\%$ strain at a speed of 10 mm min⁻¹ for over 10 cycles. Then, the output voltage amplitude and polarity as a function of the imposed compressive strains (i.e., strain rise from 1 to 50%, at a constant speed of 10 mm/min) were directly collected by the electromechanical workstation and repeated at least 3 times. Voltage relaxation experiments were further carried out by applying a constant displacement of $\epsilon = 18\%$ strain during 180 s, period during which the decay in voltage is recorded. Finally, object recognition and localization experiments respectively involved the discrimination of different indenter geometries (i.e., cylindrical objects of outer diameters 4 mm and 6 mm) as well as the site of a moving-touch stimulus through the displacement of the indenter relative to the reference electrode.

Additional Techniques: Swelling (*S*) kinetics of hydrogel-based iontronics were interpreted through their mass at predetermined time intervals (*W_t*) to the mass of a dehydrated hydrogel (*W₀*), given by:

$$S(\%) = \frac{W_t - W_0}{W_0} \times 100 \quad (4)$$

Rheological measurements were performed using a rheometer MCR 302 (Anton-Paar) using a plate-plate geometry system with a 25 mm diameter. Strain sweep measurements were performed at 25 °C with a frequency of 1 Hz and a strain range between 0.01% and 100%. Transmittance of hydrogel-based iontronics was measured using a UV-Vis spectrophotometer UV-2600 (Shimadzu) in the visible 400–800 nm range.

Ionic conductivity measurements were performed using an electrochemical impedance spectroscopy with a VSP potentiostat/galvanostat (Bio-Logic Science Instruments, France). Samples were placed between two gold plates of 20 mm diameter and measurements were performed with a frequency range between 1 Hz and 200 kHz by applying a 10 mV perturbation at room temperature.

COMSOL MultiPhysics (v5.4) was used to construct a finite element simulation coupling the poroelastic solvent flow, viscoelastic relaxation of the polymer, and the applied pressure. The geometry of a rectangular gel was defined as 1 × 2 × 0.1 cm, and a circular boundary of 2 mm diameter was placed at the top surface of the gel. The circular boundary was prescribed at 10%, 30%, and 50% compressive strains, representing the indentation. The bottom side of the gel was assigned a fixed boundary condition (displacement in *x*, *y*, and *z* directions are forced zero). All other surfaces were free to deform. The fluid phase was set to be water (1 mPa s), and the polymer was set to have elastic modulus of 10 kPa. The permeability of the matrix was set to be 10⁻¹⁵ m². Pressure evolution over time was then recorded across the cross-section of the gel.

Supporting Information

Supporting Information is available from the Wiley Online Library or from the author.

Acknowledgements

We gratefully acknowledge support from the Belgian Federal Government Office of Science Policy (SSTC-PAI 6/27) as well as both Wallonia and the European Commission “FSE and FEDER”. The authors acknowledge the Interreg France-Wallonie-Vlaanderen program, 3D4Med, with the financial support of the European Regional Development Fund (ERDF). J.-M.R. is a senior research associate at F.R.S.-F.N.R.S. (Belgium).

Conflict of Interest

The authors declare no conflict of interest.

Data Availability Statement

The data that support the findings of this study are available from the corresponding author upon reasonable request.

Keywords

iontronic sensors, stacked ionic assemblies, stereolithography, touch-pressure monitoring

Received: September 8, 2022

Revised: October 24, 2022

Published online:

- [1] a) H. Souiri, H. Banerjee, A. Jusufi, N. Radacsi, A. A. Stokes, I. Park, M. Sitti, M. Amjadi, *Adv. Int. Sys.* **2020**, 2, 2000039; b) J. Heikenfeld, A. Jajack, J. Rogers, P. Gutruf, L. Tian, T. Pan, R. Li, M. Khine, J. Kim, J. Wang, *Lab Chip* **2018**, 18, 217; c) M. Amjadi, K.-U. Kyung, I. Park, M. Sitti, *Adv. Funct. Mater.* **2016**, 26, 1678.
- [2] R. Li, Q. Zhou, Y. Bi, S. Cao, X. Xia, A. Yang, S. Li, X. Xiao, *Sens. Actuators, A* **2021**, 321, 112425.
- [3] a) J. Chen, Q. Yu, X. Cui, M. Dong, J. Zhang, C. Wang, J. Fan, Y. Zhu, Z. Guo, *J. of Mat. Chem. C* **2019**, 7, 11710; b) Z. Wang, Y. Cong, J. Fu, *J. Mater. Chem. B* **2020**, 8, 3437.
- [4] a) A. Rivadeneyra, J. A. López-Villanueva, *Micromachines* **2020**, 11, 367; b) Y. Ye, C. Zhang, C. He, X. Wang, J. Huang, J. Deng, *IEEE Access* **2020**, 8, 45325.
- [5] T. Nguyen, M. Khine, *Polymers* **2020**, 12, 1454.
- [6] C. Dagdeviren, P. Joe, O. L. Tuzman, K.-I. Park, K. J. Lee, Y. Shi, Y. Huang, J. A. Rogers, *Extreme Mech Lett* **2016**, 9, 269.
- [7] a) X. Pu, M. Liu, X. Chen, J. Sun, C. Du, Y. Zhang, J. Zhai, W. Hu, Z. L. Wang, *Sci. Adv.* **2017**, 3, e1700015; b) B. Jiang, Y. Long, X. Pu, W. Hu, Z. L. Wang, *Nano Energy* **2021**, 86, 106086.
- [8] K. K. Kim, S. Hong, H. M. Cho, J. Lee, Y. D. Suh, J. Ham, S. H. Ko, *Nano Lett.* **2015**, 15, 5240.
- [9] a) C. Wan, K. Xiao, A. Angelin, M. Antonietti, X. Chen, *Adv. Int. Sys.* **2019**, 1, 1900073; b) S. Z. Bisri, S. Shimizu, M. Nakano, Y. Iwasa, *Adv. Mater.* **2017**, 29, 1607054; c) H. Chun, T. D. Chung, *Annu. Rev. Anal. Chem.* **2015**, 8, 441.
- [10] a) J.-Y. Sun, C. Keplinger, G. M. Whitesides, Z. Suo, *Adv. Mat.* **2014**, 26, 7608; b) Z. Lei, P. Wu, *Nat. Commun.* **2018**, 9, 1134; c) B. Ying, Q. Wu, J. Li, X. Liu, *Materials Horizons* **2020**, 7, 477.
- [11] a) C. Keplinger, J.-Y. Sun, C. C. Foo, P. Rothenmund, G. M. Whitesides, Z. Suo, *Science* **2013**, 341, 984; b) T. Li, G. Li, Y. Liang, T. Cheng, J. Dai, X. Yang, B. Liu, Z. Zeng, Z. Huang, Y. Luo, T. Xie, W. Yang, *Sci. Adv.* **2017**, 3, e1602045; c) M. Duduta,

- E. Hajiesmaili, H. Zhao, R. J. Wood, D. R. Clarke, *Proc. Natl. Acad. Sci. USA* **2019**, *116*, 2476.
- [12] a) B. Nie, R. Li, J. D. Brandt, T. Pan, *Lab Chip* **2014**, *14*, 1107; b) B. Nie, R. Li, J. Cao, J. D. Brandt, T. Pan, *Adv. Mater.* **2015**, *27*, 6055; c) S. G. Yoon, S. T. Chang, *J. Mater. Chem. C* **2017**, *5*, 1910; d) Q. Liu, Z. Liu, C. Li, K. Xie, P. Zhu, B. Shao, J. Zhang, J. Yang, J. Zhang, Q. Wang, C. F. Guo, *Adv. Sci.* **2020**, *7*, 2000348.
- [13] C. Yang, Z. Suo, *Nat. Rev. Mater.* **2018**, *3*, 125.
- [14] C.-C. Kim, H.-H. Lee, K. H. Oh, J.-Y. Sun, *Science* **2016**, *353*, 682.
- [15] V. Triandafilidi, S. G. Hatzikiriakos, J. Rottler, *Soft Matter* **2018**, *14*, 6222.
- [16] a) K. Sawahata, J. P. Gong, Y. Osada, *Macromol. Rapid Commun.* **1995**, *16*, 713; b) M. S. Sarwar, Y. Dobashi, E. Glitz, M. Farajollahi, S. Mirabbasi, S. Naficy, G. M. Spinks, J. D. W. Madden, *Transparent and conformal 'piezoionic' touch sensor*, SPIE, Bellingham, WA **2015**.
- [17] A. Erbas, M. Olvera de la Cruz, *ACS Macro Lett.* **2015**, *4*, 857.
- [18] a) K. Prudnikova, M. Utz, *Macromolecules* **2012**, *45*, 1041; b) K. Prudnikova, M. Utz, in *Frontiers in Sensing: From Biology to Engineering*, Springer, New York, **2012**.
- [19] a) J. Zhao, S. Han, Y. Yang, R. Fu, Y. Ming, C. Lu, H. Liu, H. Gu, W. Chen, *ACS Nano* **2017**, *11*, 8590; b) Y. Dobashi, G. Allegretto, M. S. Sarwar, E. Cretu, J. D. W. Madden, *MRS Adv.* **2016**, *1*, 63.
- [20] a) V. Woehling, G. T. M. Nguyen, C. Plesse, Y. Petel, Y. Dobashi, J. D. W. Madden, C. A. Michal, F. Vidal, *Multifunct. Mater.* **2019**, *2*, 045002; b) S. M. Villa, V. M. Mazzola, T. Santaniello, E. Locatelli, M. Maturi, L. Migliorini, I. Monaco, C. Lenardi, M. Comes Franchini, P. Milani, *ACS Macro Letters* **2019**, *8*, 414; c) Y. Liu, Y. Hu, J. Zhao, G. Wu, X. Tao, W. Chen, *Small* **2016**, *12*, 5074.
- [21] a) N. Bai, L. Wang, Q. Wang, J. Deng, Y. Wang, P. Lu, J. Huang, G. Li, Y. Zhang, J. Yang, K. Xie, X. Zhao, C. F. Guo, *Nat. Commun.* **2020**, *11*, 209; b) A. Chhetry, J. Kim, H. Yoon, J. Y. Park, *ACS Appl. Mater. Interfaces* **2019**, *11*, 3438; c) Z. He, W. Chen, B. Liang, C. Liu, L. Yang, D. Lu, Z. Mo, H. Zhu, Z. Tang, X. Gui, *ACS Appl. Mater. Interfaces* **2018**, *10*, 12816; d) S. C. B. Mannsfeld, B. C. K. Tee, R. M. Stoltenberg, C. V. H. H. Chen, S. Barman, B. V. O. Muir, A. N. Sokolov, C. Reese, Z. Bao, *Nat. Mater.* **2010**, *9*, 859.
- [22] a) A. Fiumefreddo, M. Utz, *Macromolecules* **2010**, *43*, 5814; b) P. G. d. Gennes, K. Okumura, M. Shahinpoor, K. J. Kim, *Europhys Lett* **2000**, *50*, 513; c) E. H. Frank, A. J. Grodzinsky, *J. Biomech.* **1987**, *20*, 615.
- [23] T. B. H. Schroeder, A. Guha, A. Lamoureux, G. VanRenterghem, D. Sept, M. Shtein, J. Yang, M. Mayer, *Nature* **2017**, *552*, 214.
- [24] a) M. R. Khosravani, T. Reinicke, *Sens. Actuators, A* **2020**, *305*, 111916; b) C. Liu, N. Huang, F. Xu, J. Tong, Z. Chen, X. Gui, Y. Fu, C. Lao, *Polymers* **2018**, *10*, 629; c) Y. Xu, X. Wu, X. Guo, B. Kong, M. Zhang, X. Qian, S. Mi, W. Sun, *Sensors* **2017**, *17*, 1166.
- [25] a) J. Odent, S. Vanderstappen, A. Toncheva, E. Pichon, T. J. Wallin, K. Wang, R. F. Shepherd, P. Dubois, J.-M. Raquez, *J. Mater. Chem. A* **2019**, *7*, 15395; b) C. K. Chua, K. F. Leong, *3D Printing and Additive Manufacturing: Principles and Applications*, World Scientific, Singapore, **2015**; c) L. Gibson, D. Rosen, B. Stucker, *additive manufacturing technologies: 3D Printing, Rapid Prototyping, and Direct Digital Manufacturing*, Springer, New York, **2015**.
- [26] S. E. Root, C. W. Carpenter, L. V. Kayser, D. Rodriguez, D. M. Davies, S. Wang, S. T. M. Tan, Y. S. Meng, D. J. Lipomi, *ACS Omega* **2018**, *3*, 662.
- [27] L. W. Hill, *Prog. Org. Coat.* **1997**, *31*, 235.
- [28] Y. Dobashi, D. Yao, Y. Petel, T. N. Nguyen, M. S. Sarwar, Y. Thabet, C. L. W. Ng, E. Scabeni Glitz, G. T. M. Nguyen, C. Plesse, F. Vidal, C. A. Michal, J. D. W. Madden, *Science* **2022**, *376*, 502.
- [29] Y. Marcus, *J. Chem. Soc., Faraday Trans.* **1991**, *87*, 2995.
- [30] P. G. de Gennes, K. Okumura, M. Shahinpoor, K. J. Kim, *Europhys. Lett.* **2000**, *50*, 513.
- [31] a) M. L. White, *J. Phys. Chem.* **1960**, *64*, 1563; b) C. A. Grattoni, H. H. Al-Sharji, C. Yang, A. H. Muggeridge, R. W. Zimmerman, *J. Colloid Interface Sci.* **2001**, *240*, 601.
- [32] Z. Zhu, L. Chang, T. Horiuchi, K. Takagi, A. Aabloo, K. Asaka, *J. Appl. Phys.* **2016**, *119*, 124901.